Numerical modeling of shock waves in biomedicine

By S. Adami†, J. Kaiser†, N. A. Adams† AND I. Bermejo-Moreno‡

We have developed a multi-phase compressible fluid solver that can handle shock waves efficiently and accurately. Using a level set formulation to treat sharp interfaces and employing multi-resolution techniques, we can study complex shock-bubble interactions. In this work, shock-induced bubble collapse interactions near a deformable interface are presented as a model for a simplified extracorporeal shock-wave lithotripsy experiment. The conservative sharp-interface method was successfully validated for free-field collapse and non-spherical collapse near solid walls. We observe a systematic small deviation of our results compared with that of the diffuse-interface method from the literature.

1. Introduction

Fluid-dynamic interaction mechanisms and processes are essential to biotechnology and biomedicine. An important example is kidney stone lithotripsy, the side-effects of which are precursors to many other more recently proposed and pursued therapeutical approaches to improve drug delivery or to treat cancer (Coussios & Roy 2008; Stride *et al.* 2010).

Among the most interesting biomedical phenomena driven by shock interactions is sonoporation, where acoustic cavitation of microbubbles leads to temporary small-scale cell membrane perforations, see, e.g., Zhong *et al.* (2011) or Ohl *et al.* (2006). At the core of such processes is the generation, by bubble collapse, of highly localized shock waves that interact with ambient fluid and tissue. Such extremely small-scale yet high-energy events enable in situ control of therapeutical fluid processes with high precision and minimal side effects. The overarching goal of our research is to develop for biological applications innovative nanoscale processes that harness shock interactions in living organisms.

Experimental investigations of bubble collapse challenge scientists owing to the small spatial and, especially, temporal scales involved. Among others, Kodama & Tomita (2000) studied the collapse of gas bubbles near a gelatin surface and identified the collapse-induced liquid jet to hit and penetrate the gelatin surface. Ohl *et al.* (2006) estimated the shear stress due to the liquid jet and related it to the probability of cell membrane perforation. Alternatively, instead of measuring and visualizing, e.g., the liquid jet formation itself, the resulting effect on cells, such as increased molecular uptake of a drug (Ohl *et al.* 2006) or cell viability (Karshafian *et al.* 2009), is monitored.

Given the complexity of experimental investigations, numerical simulations can give new insights into the physics of shock-bubble interactions. In the past, different numerical methods, e.g., boundary integral methods (Calvisi *et al.* 2008) and finite volume methods (Johnsen & Colonius 2006), were applied to study bubble collapse near undeformable walls. Using the ghost fluid method, some groups have studied the deformation of a soft wall and the reflection of the pressure wave on the boundary (Kobayashi *et al.* 2011;

† Technical University of Munich, Germany
‡ Aerospace and Mechanical Engineering Department, University of Southern California

Takahira *et al.* 2008). In this paper we present our first results for a generic configuration, resembling the basic mechanism of cell membrane poration by shock-wave impact, where a gas bubble collapse near a compliant wall is initiated by the impact of a planar shock wave. The compliant wall is modeled as a gel-like fluid and represents simplified cell membrane material. We use a WENO-5 discretization scheme that combines accurate shock capturing and numerical robustness together with a level-set-based conservative interface method for compressible flows (Hu *et al.* 2006). Computational efficiency for high-resolution simulations is improved by the use of a multi-resolution algorithm, see Han *et al.* (2014).

In this work we compare the simulation results of a shock-bubble interaction near a solid wall and a deformable gelatin interface using our sharp-interface method with results from literature. First, the Rayleigh bubble collapse of a single bubble in a free-field is compared with the analytical collapse time. Then, the non-spherical bubble collapse near a solid wall is compared with findings from Johnsen & Colonius (2008). Finally, the dynamics of the bubble collapse in the presence of a deformable gelatin interface are compared with findings from Kobayashi *et al.* (2011).

In Sections 2 and 3 we introduce the governing equations and briefly describe the numerical method. Section 4 introduces the problem setup and Section 5 presents the simulation results and compares them with findings from the references. Concluding remarks are given in Section 6.

2. Governing equations

Neglecting viscous dissipation, the shock-bubble interaction is modeled with the compressible Euler equations in axi-symmetric form

$$\frac{\partial \mathbf{U}}{\partial t} + \frac{\partial \mathbf{F}\left(\mathbf{U}\right)}{\partial r} + \frac{\partial \mathbf{G}\left(\mathbf{U}\right)}{\partial z} = \mathbf{S}\left(\mathbf{U}\right), \tag{2.1}$$

where t, r and z denote the time, the radial coordinate direction and the axial coordinate direction, respectively. The solution state vector of the conservative variables density ρ, momentum ρu and ρv and energy $E = \rho e + \frac{1}{2}\rho\left(u^2 + v^2\right)$ together with the radial and axial fluxes $\mathbf{F}\left(\mathbf{U}\right)$ and $\mathbf{G}\left(\mathbf{U}\right)$ is

$$\mathbf{U} = \begin{bmatrix} \rho \\ \rho u \\ \rho v \\ E \end{bmatrix}, \ \mathbf{F}\left(\mathbf{U}\right) = \begin{bmatrix} \rho u \\ \rho u^2 + p \\ \rho uv \\ u\left(E + p\right) \end{bmatrix} \text{ and } \ \mathbf{G}\left(\mathbf{U}\right) = \begin{bmatrix} \rho v \\ \rho uv \\ \rho v^2 + p \\ v\left(E + p\right) \end{bmatrix}. \tag{2.2}$$

The velocity components in the radial and axial directions are $u = u\left(r, z\right)$ and $v = v\left(r, z\right)$. The geometric source term due to the axi-symmetric formulation of the conservation law in Eq. (2.1) is given by

$$\mathbf{S}\left(\mathbf{U}\right) = -\frac{1}{r} \begin{bmatrix} \rho u \\ \rho u^2 \\ \rho uv \\ u\left(E + p\right) \end{bmatrix}. \tag{2.3}$$

To close the system, the stiffened equation-of-state (Harlow & Amsden 1971)

$$p\left(\rho, e\right) = \left(\gamma - 1\right)\rho e - \gamma B \tag{2.4}$$

Material	ρ [kg/m^3])	γ [-]	B [Pa]
Air	1.2	1.4	0.
Water	998.6	4.4	6.0×10^8
Gelatin	1061.0	4.04	6.1×10^8
Stone	1546.0	1.66	1.12×10^{10}

TABLE 1. Material parameters

is used, where γ and B are numerical coefficients specific to each fluid. This EOS is advantageous for the given problem since all three immiscible phases (gas, surrounding water and gelatin) can be represented using this relation by adjusting the numerical parameters γ and B. Table 1, taken from Kobayashi *et al.* (2011), gives the parameters for each material. The speed-of-sound c_s for each material is obtained from

$$c_s = \sqrt{\frac{\gamma\,(p+B)}{\rho}} \ . \tag{2.5}$$

Note that using the stiffened gas equation-of-state for water results in a slightly overpredicted speed-of-sound for the liquid phase ($c_L = 1647$ m/s).

3. Numerical method

The governing equations are discretized with Cartesian finite volumes and a Riemann solver is used to calculate the fluxes between cells. A fifth-order WENO shock-capturing scheme is used and the time integration employs a second-order Runge-Kutta scheme with local time stepping (Han *et al.* 2014).

3.1. *Level set*

A level set function φ is evolved in time in addition to the governing Eq. (2.1) to track the motion of the interface. The signed distance function $\varphi\,(\mathbf{x}, t)$ defines the location of the interface by the zero level set and follows the linear advection equation

$$\frac{\partial \varphi}{\partial t} + u\frac{\partial \varphi}{\partial r} + v\frac{\partial \varphi}{\partial z} = 0 \ . \tag{3.1}$$

Re-initialization of the level set function is performed according to Sussman *et al.* (1994) to maintain the signed distance property during the evolution of the interface. The conservative interface method for compressible flows by Hu *et al.* (2006) is used for cells that are cut by the interface.

Presently, a single level set function is used to identify the location of the interface between the bulk water phase and a second immiscible phase. Depending on the global position of the interface the phase properties of the second phase can be modified. This approach allows us to consider the three-phase problem of a gas bubble in water near a gelatin interface using a single level set function. However, the position-based switch of the phase properties works only for non-penetrating phases and limits our investigation to early-stage collapse effects on the gelatin interface deformation. We are currently extending our method for full three-phase (and more) interactions with our recently developed multi-material level set approach (Pan *et al.* 2016).
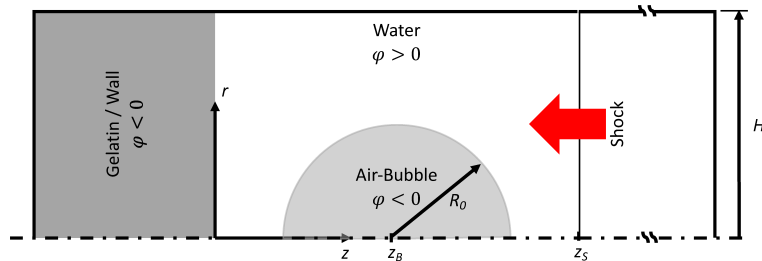
FIGURE 1. Sketch of the simulation setup.

3.2. *Multi-resolution*

A multi-resolution (MR) algorithm that follows Han *et al.* (2014) is used to achieve high computational efficiency for high-resolution simulations. The smoothness of the flow field is estimated by comparing the numerical solution on the current level of refinement with its interpolation on a coarse grid. If that so-called detail is smaller than a specified threshold, then the coarse grid is deemed sufficient to represent the solution at the given accuracy. The level-dependent threshold ϵ_l for the details on the level l is

$$\epsilon_l = 2^{d(l-L_{max})}\epsilon_{ref} \ , \tag{3.2}$$

where d is the number of spatial dimensions, L_{max} the maximum number of grid refinements and ϵ_{ref} the reference tolerance on the finest grid. If not stated otherwise, we used $L_{max} = 6$ with $\epsilon_{ref} = 0.01$. Further information on the scheme can be found in Han *et al.* (2014) or the original work of Harten (1995).

4. Problem setup

The setup of the numerical problem is sketched in Figure 1. At $z = 0$, either a solid wall or the interface between water and gelatin will be considered independently. The initial shock front position is $z_S = 2.6\ R_0$ and the bubble is located at $z_B = 1.2\ R_0$. The gelatin thickness is $z_g = 6.8\ R_0$ and the end of the pressure pulse is at $z_{max} = z_s + 30.6\ R_0$. In the radial direction the domain size is $H = 4\ R_0$. For the non-spherical bubble collapse case (Section 5.2) we use $H = 14.2\ R_0$.

The Rayleigh collapse simulations (Section 5.1) are performed with a simplified setup without the third material and by using symmetry boundary conditions. The bubble is placed at $(z, r) = (8\ R_0, 0.0)$ and the total domain size is $z_{max} = 16\ R_0$ and $H = 8\ R_0$.

4.1. *Pressure pulse*

For the non-spherical bubble collapse near a wall a realistic lithotripter pulse

$$p\left(z' = z - z_S\right) = p_0 + 2p_s e^{-\left(\alpha\ z'/c_L\right)}\cos\left(\omega\frac{z'}{c_L} + \frac{\pi}{3}\right), \quad z \geq z_S \tag{4.1}$$

is used. The parameters α, ω and p_s are taken from Johnsen & Colonius (2008), the resulting nominal pulse width is $\sigma = 6.75$ mm and p_0 is atmospheric pressure (1013 mbar).

For the deformable interface simulations we use the slightly modified pressure pulse of
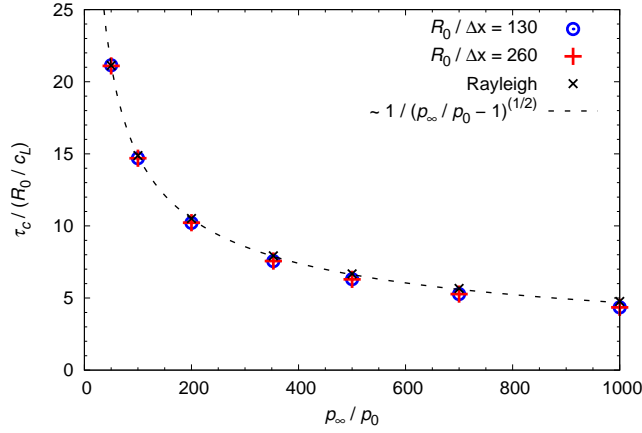
FIGURE 2. Rayleigh collapse: free-field collapse time of an isolated gas bubble in water with radius $R_0 = 0.8$ mm as a function of the non-dimensional pressure ratio p_∞/p_0.

Kobayashi *et al.* (2011)

$$p\left(z' = z - z_S\right) = 108 \text{ MPa} \cdot \exp\left[-\frac{393.9}{m}z'\right] + p_0, \quad z \geq z_S, \tag{4.2}$$

to allow for a direct comparison of the results.

5. Results

Prior to simulating the bubble collapse with a deformable gelatin interface, we present several verification cases. With increasing complexity, first, a single bubble collapse in a free-field is simulated and compared with the theoretical results of Rayleigh and second, the non-spherical bubble collapse near a solid wall is compared with results by literature Johnsen & Colonius (2008). In the last subsection the actual problem setup is simulated and compared with results by Kobayashi *et al.* (2011).

5.1. *Rayleigh collapse*

A spherical, non-condensable gas bubble in a free-field with radius $R_0 = 0.8$ mm at atmospheric pressure collapses due to increased ambient pressure p_∞ in the surrounding liquid. Depending on the initial radius R_0, the liquid density ρ_L and the pressures outside and inside the gas bubble p_∞ and p_0, the so-called Rayleigh collapse time is given by

$$\tau_c \approx 0.915\sqrt{\frac{\rho_L}{p_\infty - p_0}}R_0 \ , \tag{5.1}$$

see Brennen (1995). Figure 2 shows the trend of the collapse time for varying pressure ratios p_∞/p_0. The time is non-dimensionalized with the reference time $t_{ref} = R_0/c_L$, where c_L denotes the speed-of-sound in the liquid phase. In addition to two different resolution results the theoretical Rayleigh collapse times are plotted together with a $1/\sqrt{(p_\infty/p_0 - 1)}$ trend. The agreement between the numerical results and the theoretical collapse time is very good and the largest errors are within a few percent for very high pressure ratios. The resolution of 130 cells per bubble diameter at the finest grid level is sufficient and this setup is used for the following simulations.
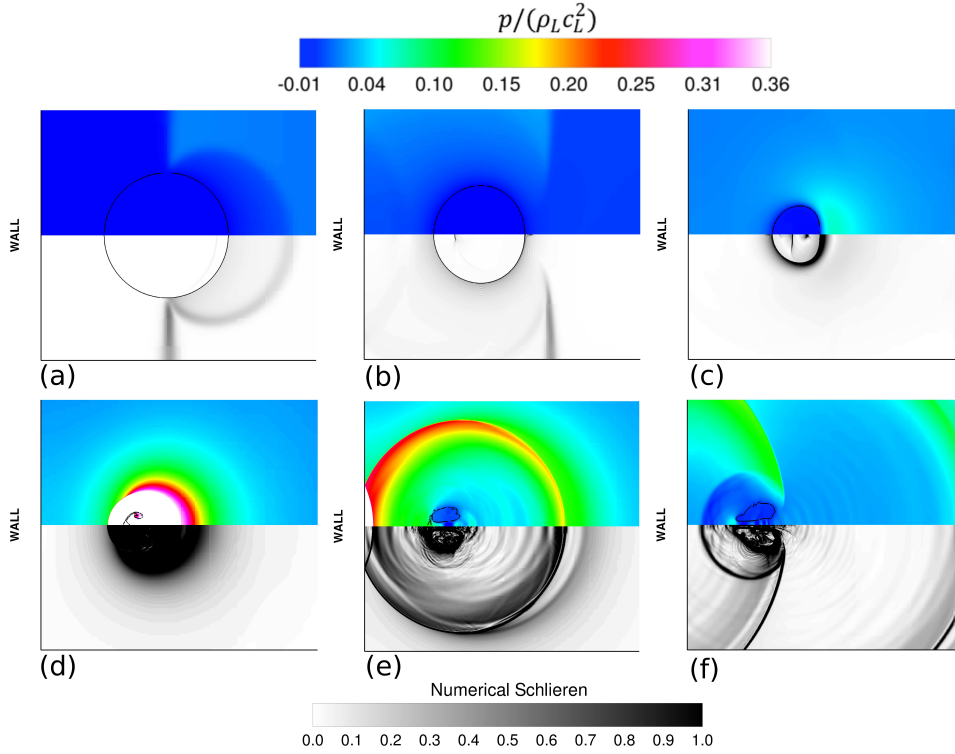
FIGURE 3. Pressure profiles (top) and numerical Schlieren (bottom) contours for the shock-induced gas bubble collapse near a wall at $tc_L/R_0 = 4.94, 9.88, 11.86, 12.85, 13.83$ and 15.15, (a) to (f).

5.2. *Non-spherical bubble collapse*

Johnsen & Colonius (2008) present the shock-induced collapse of a gas bubble near a solid wall using a very similar numerical approach (finite volume, WENO-5, stiffened gas equation-of-state, HLLC solver) but a diffuse-interface method. A bubble with initial radius $R_0 = 50 \ \mu$m is placed next to a solid wall at a distance $z_B/R_0 = 2.0$ and is exposed to the lithotripter pulse given in Eq. (4.1).

Figure 3 shows the pressure field and numerical Schlieren contours of the collapsing bubble using the presented sharp-interface method. The overall agreement with the reference is good, especially during the pre-collapse phase.

In Figure 4(a) the bubble volume and center-of-mass position are monitored. Both curves agree very well with findings by Johnsen & Colonius (2008). The interface velocities on the centerline of the bubble are shown in Figure 4(b). Here, v_j denotes the jet velocity of the interface initially facing the pressure pulse and v_d denotes the velocity of the distal interface initially facing the solid wall. Apart from the very good agreement for the pre-collapse phase the sharp-interface method obviously predicts a much stronger collapse (see the larger interface velocities during the collapse). Also, the numerical minimum bubble volume is two orders of magnitude smaller. These observations are consistent with the better interface-capturing capabilities of the sharp-interface method compared with the diffuse-interface method within the considered inviscid flow setting.

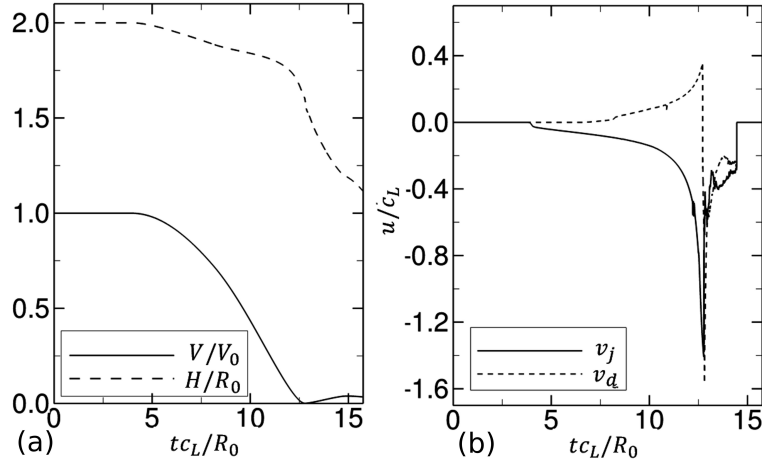Accordingly, the pressure histories at the wall at several radial distances in Figure

FIGURE 4. (a) Time histories of the normalized bubble volume (V/V_0) and wall stand-off distance (H/R_0) and (b) velocities of the jet (v_j) and distal side (v_d) for the shock-induced collapse.
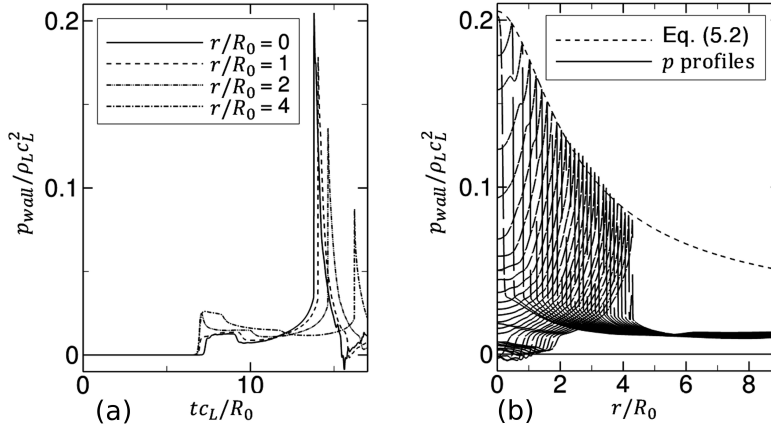

FIGURE 5. Wall impact pressure profiles: (a) temporal pressure profiles at the wall for four different radial coordinates, (b) spatial pressure profiles along the wall for preceding time.

5(a) show larger peak values. In Figure 5(b) the spatial pressure profiles along the wall interface are plotted for increasing time. As shown by Johnsen & Colonius (2008), the maximum wall pressures follow a purely geometrical decay given by

$$p_{wall}\left(\frac{r}{R_0}\right) = \frac{a}{\sqrt{z_C^2 + (r/R_0)^2}} + b \, , \qquad (5.2)$$

where z_C is the collapse distance to the wall and a and b are parameters that can be determined using two spatial pressure profiles. Despite the overall larger pressure peaks, which relate to the difference in the interface treatment, our results agree very well with the reference results.
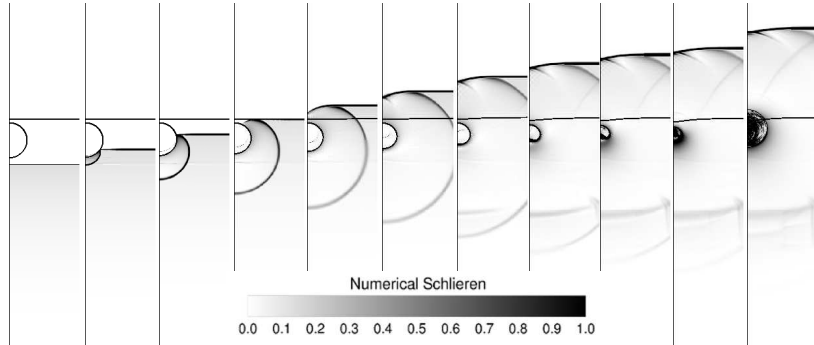
FIGURE 6. Numerical Schlieren contours of the shock-induced bubble collapse near a gelatin interface.
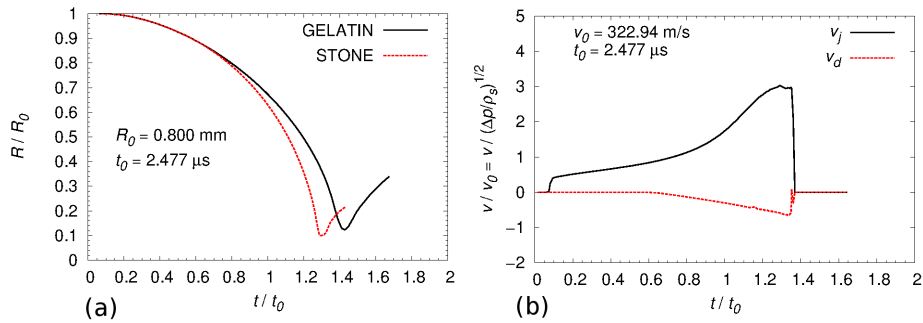

(a)

(b)

FIGURE 7. Temporal evolution of the (a) effective gas bubble radius and (b) interface velocities for the gelatin setup.

5.3. *Bubble collapse near the deformable gelatin interface*

As a model for shock-wave lithotripsy, Kobayashi *et al.* (2011) studied the interaction of a deformable tissue phase with a shock-induced collapsing gas bubble. The problem setup is shown in Figure 1, and the initial bubble radius is $R_0 = 0.8$ mm. For the other geometrical parameter we refer to the problem description in Kobayashi *et al.* (2011). To compare the presented plots we mapped the numerical results to their coordinate system.

The numerical Schlieren image in Figure 6 shows the interface evolution of the gas bubble and the gelatin interface. In this visualization the shock front moves upward. When the initial shock hits the gas bubble, a reflection wave is created. Later, the original shock crosses the tissue interface without reflections as the impedance of water and gelatin is equal. At early times, the gelatin interface moves toward the gas phase. During the collapse a strong compression wave due to the waterhammer with a much larger amplitude compared to the original shock is emitted and hits the gelatin interface. Consequently, this interface is strongly accelerated and forms a cavity. This deformation seems to indicate the poration of the cell membranes due to a bubble collapse. Given the simple region-based switch in material properties, the current numerical setup breaks down as soon as the bubble interface moves into the original gelatin interface location. Therefore, we limit our analysis to the initial collapse phase.

The equivalent bubble radius over time is plotted in Figure 7(a). The time is non-dimensionalized with the equivalent Rayleigh collapse time and results are presented for two different tissue materials, i.e., gelatin and stone (see Table 1 for the material
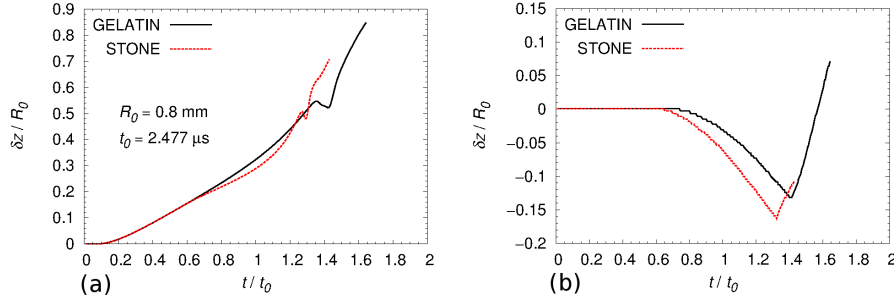
FIGURE 8. (a) Axial bubble motion and (b) tissue deformation at $r = 0$ for two different materials.

properties). The presence of a deformable interface retards the bubble collapse compared with the free-field collapse. The interface velocities v_j and v_d (for definitions see the previous subsection) for the gelatin interface are shown in Figure 7(b). The vanishing interface velocity at post-collapse times is a postprocessing artifact due to the interface breakup on the centerline of the bubble. Additionally, Figure 8 shows the axial bubble motion δz and tissue deformation at $r = 0$ for the two materials.

Comparing all presented plots with the reference results in Kobayashi *et al.* (2011) shows the same qualitative behavior, see, e.g., the characteristic difference in the axial bubble displacement between the two materials. However, the collapse is predicted at a slightly shorter timescale by our conservative sharp-interface method. The smallest bubble radius in the presented results occurs at $t/t_0 \approx 1.4$ for the gelatin case, whereas the reference results show a minimum radius at $t/t_0 \approx 1.6$. These systematic differences are currently under investigation.

6. Conclusions

We have presented a sharp-interface method for compressible flows that is applied to the problem of shock-induced bubble collapse near a deformable interface. Very good agreement is found for the free-field Rayleigh collapse. The effect of the chosen interface method is visible in the example of a non-spherical collapse near a solid wall, where the sharp-interface model predicts larger peak pressure amplitudes but overall comparable interface dynamics. The deformable interface interaction presents systematically higher intensities and shorter timescales compared with a diffuse interface method. Although such observations may be related to the expected benefits of sharp and conservative interface interaction methods, the issue requires further investigations. In the future we will extend our simulations to a fully three-dimensional setup and further analyze the differences between the different numerical methods.

REFERENCES

Brennen, C. E. 1995 *Cavitation and Bubble Dynamics. Oxford engineering science series* 44. Oxford University Press.

Calvisi, M. L., Iloreta, J. I. & Szeri, A. J. 2008 Dynamics of bubbles near a rigid surface subjected to a lithotripter shock wave. Part 2. Reflected shock intensifies non-spherical cavitation collapse. *J. Fluid Mech.* **616**, 63.

Coussios, C. C. & Roy, R. A. 2008 Applications of acoustics and cavitation to non-invasive therapy and drug delivery. *Annu. Rev. Fluid Mech.* **40**, 395–420.

Han, L., Hu, X. & Adams, N. 2014 Adaptive multi-resolution method for compressible multi-phase flows with sharp interface model and pyramid data structure. *J. Comput. Phys.* **262**, 131–152.

Harlow, F. & Amsden, A. 1971 *Fluid dynamics.* Tech. Rep. LANL Monograph LA-4700.

Harten, A. 1995 Multiresolution algorithms for the numerical solution of hyperbolic conservation laws. *Comm. Pur. Appl. Math.* **48**, 1305–1342.

Hu, X., Khoo, B., Adams, N. & Huang, F. 2006 A conservative interface method for compressible flows. *J. Comput. Phys.* **219**, 553–578.

Johnsen, E. & Colonius, T. 2006 Implementation of WENO schemes in compressible multicomponent flow problems. *J. Comput. Phys.* **219**, 715–732.

Johnsen, E. & Colonius, T. 2008 Shock-induced collapse of a gas bubble in shockwave lithotripsy. *J. Acoust. Soc. Am* **124**, 2011.

Karshafian, R., Bevan, P. D., Williams, R., Samac, S. & Burns, P. N. 2009 Sonoporation by ultrasound-activated microbubble contrast agents: Effect of acoustic exposure parameters on cell membrane permeability and cell viability. *Ultrasound Med. Biol.* **35**, 847–860.

Kobayashi, K., Kodama, T. & Takahira, H. 2011 Shock wave–bubble interaction near soft and rigid boundaries during lithotripsy: Numerical analysis by the improved ghost fluid method. *Phys. Med. Biol.* **56**, 6421–6440.

Kodama, T. & Tomita, Y. 2000 Cavitation bubble behavior and bubble–shock wave interaction near a gelatin surface as a study of in vivo bubble dynamics. *Appl. Phys. B* **70**, 139–149.

Ohl, C.-D., Arora, M., Ikink, R., de Jong, N., Versluis, M., Delius, M. & Lohse, D. 2006 Sonoporation from jetting cavitation bubbles. *Biophys. J.* **91**, 4285–4295.

Pan, S., Hu, X. Y. & Adams, N. A. 2016 A multi-region approach for evolving interface networks based on local level sets. *J. Comput. Phys.* (submitted).

Stride, E. P., Coussios, C. C. & Wells, P. N. T. 2010 Cavitation and contrast: The use of bubbles in ultrasound imaging and therapy. *P. I. Mech. Eng. H.* **224**, 171–191.

Sussman, M., Smereka, P. & Osher, S. 1994 A level set approach for computing solutions to incompressible two-phase flow. *J. Comput. Phys.* **114**, 146–159.

Takahira, H., Matsuno, T. & Shuto, K. 2008 Numerical investigations of shock–bubble interactions in mercury. *Fluid. Dyn. Res.* **40**, 510–520.

Zhong, W., Sit, W. H., Wan, J. M. & Yu, A. C. 2011 Sonoporation induces apoptosis and cell cycle arrest in human promyelocytic leukemia cells. *Ultrasound Med. Biol.* **37**, 2149–2159.